journal of the mechanical behavior of biomedical materials 153 (2024) 106468

Contents lists available at ScienceDirect

Journal of the Mechanical Behavior of Biomedical Materials

journal homepage: www.elsevier.com/locate/jmbbm

A numerical study of dehydration induced fracture toughness degradation in human cortical bone

Mihee Shin [a], Penny J. Martens [b], Thomas Siegmund [c], Jamie J. Kruzic [a], Bernd Gludovatz [a,*]

[a] School of Mechanical and Manufacturing Engineering, University of New South Wales (UNSW Sydney), Sydney, NSW, 2052, Australia
[b] Graduate School of Biomedical Engineering, University of New South Wales (UNSW Sydney), Sydney, NSW, 2052, Australia
[c] School of Mechanical Engineering, Purdue University, West Lafayette, IN, 47907, USA

ARTICLE INFO

Keywords:
Bone
Microstructure
Cement line
Mechanical characterization
Deformation and fracture toughness
Crack resistance curve behavior

ABSTRACT

A 2D plane strain extended finite element method (XFEM) model was developed to simulate three-point bending fracture toughness tests for human bone conducted in hydrated and dehydrated conditions. Bone microstructures and crack paths observed by micro-CT imaging were simulated using an XFEM damage model. Critical damage strains for the osteons, matrix, and cement lines were deduced for both hydrated and dehydrated conditions and it was found that dehydration decreases the critical damage strains by about 50%. Subsequent parametric studies using the various microstructural models were performed to understand the impact of individual critical damage strain variations on the fracture behavior. The study revealed the significant impact of the cement line critical damage strains on the crack paths and fracture toughness during the early stages of crack growth. Furthermore, a significant sensitivity of crack growth resistance and crack paths on critical strain values of the cement lines was found to exist for the hydrated environments where a small change in critical strain values of the cement lines can alter the crack path to give a significant reduction in fracture resistance. In contrast, in the dehydrated state where toughness is low, the sensitivity to changes in critical strain values of the cement lines is low. Overall, our XFEM model was able to provide new insights into how dehydration affects the micromechanisms of fracture in bone and this approach could be further extended to study the effects of aging, disease, and medical therapies on bone fracture.

1. Introduction

Adult human cortical bone consists of hydroxyapatite mineral crystals, collagen, and water arranged in a hierarchical structure whereby mineralized collagen fibers are arranged in layers of cylindrical lamellae forming osteons with Haversian canals in their center (Weiner and Wagner, 1998). The osteons, emerging from the bone remodeling processes, are aligned primarily parallel to the long bone axis, and are embedded in the interstitial bone matrix. The interfaces between the osteons and matrix are known as cement lines and they play an important role in the bone fracture process by acting as deflection paths for cracks (Lin et al., 2016; Tang et al., 2015; O'Brien et al., 2007; Zimmermann et al., 2009; Zimmermann et al., 2010). Additionally, water is highly important to the fracture resistance in bone, and it has been shown that dehydrated bone is embrittled (Broz et al., 1993; Nyman et al., 2013; Yan et al., 2008; Melvin and Evans, 1973; Kahler et al., 2003; Shin et al., 2022). At the collagen level, water is thought to provide a plasticizing effect from the presence of the ordered hydration layer of water molecules occupying hydrogen bonding sites along the collagen molecules and from hydrogen bonded water ''bridges'' that span between the collagen molecules (Broz et al., 1993; Granke et al., 2015; Nalla et al., 2006a; Nalla et al., 2005). While the loss of this plasticizing effect is certainly a contributing factor to the loss in fracture toughness of dehydrated bone (Lucksanasombool et al., 2001; Shin et al., 2022; Smith et al., 2011), it does not take into account the importance of changes in the hierarchical structure of bone, and very little is known about how dehydration affects the micromechanisms of bone fracture at the coarser hierarchical levels.

In this regard, computational fracture mechanics models can be useful tools to provide mechanistic insight in the fracture process in bone (Ural, 2020). For example, Mischinski and Ural have applied a cohesive zone finite element modeling method to investigate crack propagation mechanisms and the factors controlling the crack trajectory with both a single osteon model (Mischinski and Ural, 2011) and a

* Corresponding author.
E-mail address: b.gludovatz@unsw.edu.au (B. Gludovatz).

https://doi.org/10.1016/j.jmbbm.2024.106468
Received 15 October 2023; Received in revised form 21 January 2024; Accepted 15 February 2024
Available online 16 February 2024

whole bone model (Ural and Mischinski, 2013). Such work revealed the significant impact of low cement line strength on microscale toughening and the fracture toughness of cortical bone. However, one limitation of cohesive zone finite element models is that these models require the placement of cohesive zone elements along likely crack paths and thus do not allow full freedom for the crack to decide its path. The extended finite element method (XFEM) (Belytschko et al., 2001; Belytschko and Black, 1999) is one approach to overcome this issue by incorporating the theory of partition of unity into the standard finite element method (FEM) (Melenk and Babuška, 1996). The XFEM has been adopted into cortical bone models to investigate the fracture micromechanisms within the microstructure (Broz et al., 1993; Nyman et al., 2013; Yan et al., 2008; Melvin and Evans, 1973; Kahler et al., 2003; Shin et al., 2022; Li et al., 2013; Abdel-Wahab et al., 2012; Vergani et al., 2014). Recently, two XFEM based studies have shown great promise in predicting realistic crack paths for a theoretical single osteon geometry without predefined paths (Gustafsson et al., 2019a; Marco et al., 2018). Building on such successes, more complex microstructural models have been developed using micro-computed tomography (micro-CT) images of bone microstructure and they have found good agreement with experimental fracture results (Yadav et al., 2021).

Despite numerous successes using numerical studies to help understand the bone fracture process, few studies have investigated the role of water hydration. Tamilselvan and Zhang (2002) investigated the effect of water content on tensile tests by incorporating the effect of water through changing the Young's modulus of the mineralized tissue interface without including coarser microstructural features such as osteons and cement lines. Similarly, Maghsoudi-Ganjeh et al. (2020) employed a nanoscale bone model using a 2D cohesive method to show how dehydration changes the interface behavior of the collagen at sub-micrometer levels and affects the deformation behavior of wet and dry bone. Finally, Pereira et al. (2012) investigated the effect of hydrating conditions on mode I crack propagation experimentally and numerically using a homogeneous finite element model without the distinct cement lines, osteons, and matrix that are present in the bone microstructure.

In our previous work (Shin et al., 2022), the effect of dehydration by testing the bone in an electron microscope revealed a significant impact on the crack initiation and growth toughness of both human and sheep cortical bone. In this study, we develop two-dimensional XFEM models constructed using the microstructures measured from micro-CT images of human bone samples tested in different environments (Shin et al., 2022). By calibrating the models to the experimental results, critical damage strains for the osteons, cement lines, and the interstitial matrix were determined for the various test environments during crack initiation and the early stages of crack extension. Finally, a parametric study was performed to provide new insight into the relative effect of the various critical damage strain values on the fracture resistance of bone in the different hydration states.

2. Methods

2.1. Model geometry and microstructures

Experimental data used in this study was taken from our previous work (Shin et al., 2022) and full details of the fracture experiments, the various scanning electron microscope (SEM) condions, and the micro-CT imaging procedures can be found there. Briefly, fracture experiments were performed in three-point bending in general accordance with ASTM standard E1820 (ASTM Standard E1820, 2020) using single edge-notched bend, SEN(B), samples cut from the femoral cortical bone of a 46-year-old white male with no record of bone disease, as shown in Fig. 1a. Beam dimensions were thickness, $B \approx 2$ mm, width, $W \approx 2$ mm, length, $L \approx 10$ mm. A razor blade was used to place an initial micronotch into each sample with a notch root radius between 5 and 10 μm and length, $a \approx 0.8$ mm, with the crack growth direction oriented along the radius of the femur bone and the crack plane perpendicular to the bone long axis. This corresponds to the most common orientation for physiological bone fractures and is defined as the L-R cracking orientation in ASTM standard E1823 (ASTM E1823-20a, 2020), where L refers to the crack plane orientation and R refers to the crack propagation direction. The samples were continuously hydrated during preparation and immersed in Hanks' Balanced Salt Solution (HBSS) at ambient temperatures for 24 h prior to testing. Samples were grouped and tested in four different environments: i) under high vacuum conditions in an SEM (HV-SEM), ii) in a variable air pressure environmental SEM (VP-ESEM),

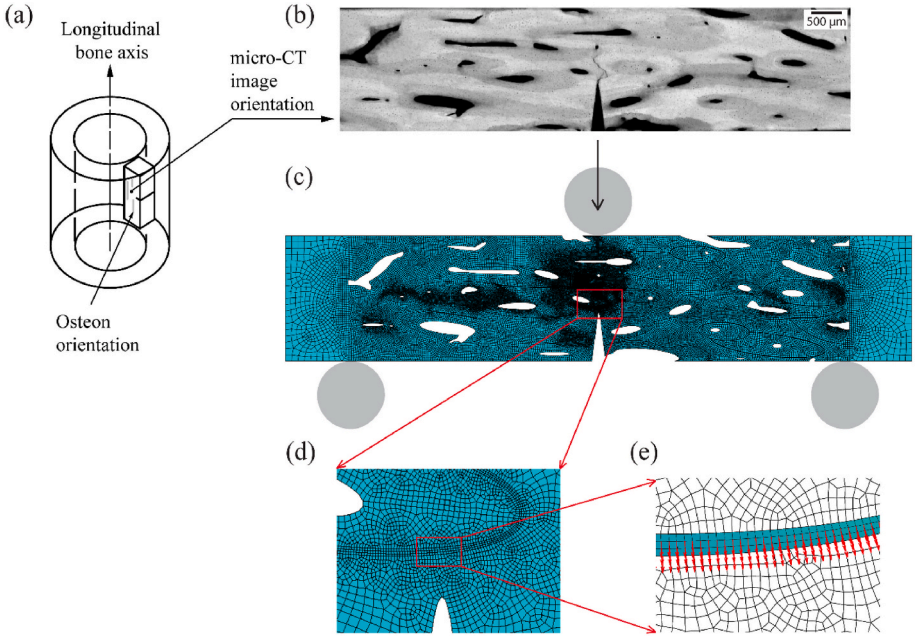

Fig. 1. (a) Schematic of the single edge-notched bend samples that were obtained from the human femur; (b) micro-CT slice used for an XFEM damage model; (c) schematic of a three-point bending setup shown with a discretized 2D model; (d) an enlarged view of elements near the initial notch; (e) an enlarged view of elements of cement lines (in turquoise) and outward normal vectors along the cement lines (in red).

iii) in a variable water vapor pressure ESEM (WV-ESEM), and iv) in ambient air (23 °C, 20–40% relative humidity) while being hydrated with HBSS. Details of the testing conditions are listed in Table 1. Samples tested in an SEM were equilibrated to the environmental conditions for 3–5 min prior to testing. After the fracture tests were completed, one representative sample from each test group that was not completely fractured was scanned using micro-CT with a voxel size of 1.5 μm to observe the detailed crack path within the microstructure.

At least one representative slice was taken from each of the four micro-CT scans (each stack contains ~300 slices), as shown in Fig. 1b, using ImageJ 1.8.0 software (National Institutes of Health, USA). These selected slices were subjected to binarization and masking processes to generate outline templates for sketching contours of model domains for each testing condition using the SolidWorks 2017 software package (Dassault Systems, USA). The image slices were segmented into three phases: osteons, interstitial matrix, and cement lines. The cement lines were allocated along the osteon boundaries. This allocation was based on the assumption that each osteon is associated with a cement line, as cement lines were not clearly distinguishable in the micro-CT images used, while osteon boundaries and the interstitial matrix were distinguishable due to the differences in their pixel intensities. In the allocation process, the achievable minimum thickness was constrained to a range of 5–10 μm due to the geometrical complexity of the osteons. Both initial notches and Haversian canals were marked as empty regions. The resulting geometry was then loaded into Abaqus software (V2021, Dassault systems, USA) as a geometry input file based on which the 2D fracture analysis models were built. In total, six microstructural models were developed corresponding to samples tested in the various experimental environments: three samples tested in air, and one each for HV-SEM, VP-ESEM, and WV-ESEM.

Using the meshing tools in the software Abaqus, plane strain 4-noded quadrilateral elements (CPE4R) with reduced integration were used to construct a 3-phase model of osteons, interstitial matrix, and cement lines, as shown in Fig. 1c. Based on the outcomes of a mesh sensitivity analysis, shown in the supplementary information, the models were discretized with a non-uniform mesh of ~50,000 elements. While most parts of the mesh were constructed with elements of 5–20 μm size, regions with cement lines were built with elements of 3–5 μm size such that a minimum of two elements were present across the thickness of the cement lines. Structured meshes were used in the cement lines near the initial notch, whereas unstructured meshes were used for the rest of the models. Example images of a mesh from a cement line ahead of a notch are shown in Fig. 1d and e. In Fig. 1e, the elements in the cement line are highlighted in turquoise and outward normal vectors which were used for failure criteria are shown as red arrows. For fracture analyses, three-point bending tests under quasi-static loading were simulated to match the experimental configuration. Displacement-controlled loading was applied to the center of the top boundary, in line with the initial micronotch, and the bottom was supported by two rigid pins modeled as analytical rigid bodies with a diameter of 1.5 mm at a span of 8 mm, as shown in Fig. 1c.

2.2. Extended finite element method (XFEM) damage model framework

An XFEM damage model that was introduced by Gustafsson et al. (2019a) was used to simulate crack initiation and propagation in the three-point bending tests. The model used a set of enrichment functions for the simulation of both crack initiation and growth. With this method, 2D microstructure models were developed in Abaqus (V2021, Dassault systems, USA), where the elements near the initial notch area over a size of approximately 1.0 × 0.5 mm^2 were selected for arbitrary crack growth under loading. The fracture process was simulated based on the traction-separation law that includes damage initiation and evolution laws. During loading, the damage criteria were continuously evaluated. When a damage initiation criterion was met, these elements were partitioned into two parts and a damage evolution law with linear softening behavior was applied until the strain energy release rates reached critical values to full separation and crack formation or advance.

The XFEM damage model uses two criteria for crack initiation; the maximum principal strain criterion (MAXPE) was applied to the matrix, osteon, and cement line phases, and, additionally, the quadratic nominal strain criterion (QUADE) was applied to the cement lines. Simultaneously using two failure criteria for the cement lines enabled the simulation of experimentally observed crack paths either along or penetrating the cement lines. The MAXPE fracture criterion, f_{MAXPE} is defined as

$$f_{\mathrm{MAXPE}} = \left\{\frac{\varepsilon_{\max}}{\varepsilon^0_{\max}}\right\}, \tag{1}$$

where $\varepsilon_{\max}$ is the maximum principal strain and $\varepsilon^0_{\max}$ is the critical damage principal strain. A crack starts to grow when $f_{\mathrm{MAXPE}} > 1$ in a direction where the maximum principal orientation is given as a normal vector. The QUADE fracture criterion, f_{QUADE} is defined as

$$f_{\mathrm{QUADE}} = \left\{\frac{\varepsilon_n}{\varepsilon^0_n}\right\}^2 + \left\{\frac{\varepsilon_s}{\varepsilon^0_s}\right\}^2, \tag{2}$$

where ε_n and ε_s are the normal and shear principal strains, respectively, and ε^0_n and ε^0_s are the critical normal and shear interface strains in the cement lines, respectively. Similar to MAXPE, a crack starts to grow when $f_{\mathrm{QUADE}} > 1$, but in a direction along the cement line as predefined normal vectors are given via a subroutine. The normal vectors of cement lines were created with MATLAB (MATLAB. version 9, 2020) based on the geometry input data and an example image of vectors – drawn as red arrows – is shown in Fig. 1e. The two criteria were implemented in the user-defined damage initiation subroutine UDMGINI for crack initiation when (f_{QUADE}, f_{MAXPE}) > 1. As a result, the MAXPE criterion allowed a crack to propagate through the cement line, and the QUADE criterion allowed for a crack to propagate along the cement line when either criterion met the condition before the other. The subroutine UDMGINI code can be found in the Supplementary Information.

2.3. Material properties

The interstitial matrix, osteons, and cement lines were modeled as linear-elastic isotropic materials. Initially, we used for each of the three components Young's moduli, *E,* reported by Yadav et al. (2021) that were obtained using nanoindentation; 23.04 ± 3.00 GPa for matrix, 16.60 ± 1.55 GPa for osteons, and 10.43 ± 4.14 GPa for cement lines. The preliminary moduli were subsequently tailored so that the obtained load-displacement curves match our experimentally determined data for the various test environments (Giner et al., 2017); the determined values are listed in Table 2. The critical strain energy release rate, $G_{c,}$ for crack initiation was obtained from the experimental test results of stress intensity, $K_{J,}$ values at the first recorded crack extension that was less than 100 μm for all test environments. The obtained G_c values were used for

Table 1
Experiment conditions of each group.

	HV-SEM	VP-ESEM	WV-ESEM	Air
Pressure/Torr (Pa)	~7.5×10^{-5} (~0.01)	~0.26 (~35)	~10 (~1333)	~760 (~101,325)
Temperature/°C	~23 (Ambient temperature)			

Table 2
Material properties model input of microstructural phases of cortical bone used for a fracture analysis study of a 3-phase model in different test environments.

Material Properties	Test condition	Matrix	Osteons	Cement lines
E (GPa)	Air/WV/HV/VP-SEM	19.02 ± 4.02	13.70 ± 2.90	8.61 ± 1.82
Poisson's ratio	Air/WV/HV/VP-SEM	0.3	0.3	0.3
Critical energy release rate (kJ/m^2)	Air	1.128	1.128	0.564
	WV-ESEM	0.036	0.036	0.018
	HV-SEM	0.027	0.027	0.014
	VP-ESEM	0.024	0.024	0.012
Initial estimates of critical damage strain	Air/ESEM/HV/VP	0.00264	0.00264	0.00132

the matrix and the osteons, whereas $G_c/2$ was applied to the cement line interfaces as has been done in previous studies (Ural and Mischinski, 2013; Yadav et al., 2021). An initial value of critical damage strain for matrix and osteons in all test environments was adopted from the ultimate strain reported by McCalden et al. (1993); half this value was used for the cement line. All material parameters are summarized in Table 2.

2.4. Critical damage strain determination

To determine the critical damage initiation strains, ε^0, that correspond to the experimental fracture toughness results, the XFEM damage models were analyzed iteratively. Initially, the critical damage initiation strains for the MAXPE criteria of both matrix and osteons, ε^0_m and ε^0_o, respectively, were assumed to be 0.00264, whereas 0.00132 was assumed for the MAXPE criterion of the cement lines, ε^0_{cm}, as well as for the QUADE criteria in the normal and shear directions, $\varepsilon^0_{cq\text{-}n}$ and $\varepsilon^0_{cq\text{-}s}$, respectively, of the cement lines. Our assumption of using $\varepsilon^0/2$ agrees with Yadav et al. who used half the critical stress value of both the osteons and the matrix for the cement lines (Yadav et al., 2021). This is based on numerical work by Ural and Mischinski, indicating that a lower strength of cement lines compared to the surrounding bone promotes longer crack growth along the cement lines as compared to the case where all components have the same properties (Ural and Mischinski, 2013).

During the simulations, ε^0_m and ε^0_o were assumed to be equal, as were $\varepsilon^0_{cq\text{-}n}$ and $\varepsilon^0_{cq\text{-}s}$ assumed to be equal. Numerical fracture analyses were conducted and compared with experimental results of load-displacement curves and crack propagation patterns. Analyses were iteratively repeated with increasing damage strains until the numerical study results agreed with experimental results for the various test environments by visual comparison of load-displacement curves and crack profiles.

Table 3
XFEM model numbers and corresponding study environments, along with the geometry model environment used in the experiment.

XFEM study environment	Model number	Experiment environment
Hydrated Air	1	Air 1
	2	Air 2
	3	Air 3
	4	HV-SEM
	5	VP-ESEM
	6	WV-ESEM
Dehydrated SEM	7	HV-SEM
	8	VP-ESEM
	9	WV-ESEM
	10	Air 1
	11	Air 2
	12	Air 3

2.5. Simulations of changing environments via the critical damage strains

To test if changing the critical damage strains is a viable way to represent the hydration state in the model, a computational fracture analysis was performed for each model with a different set of critical damage strains to understand their impact on both the initiation and growth of a crack. I.e., representative hydrated critical damage strains were used in the three SEM environment microstructural models (models 4–6 in Table 3), and representative dehydrated critical damage strains were used in the three air environment models (models 10–12 in Table 3). The sets of parameter values obtained from the critical damage strain determination in different environments were used for the different models 4–6 and 10–12. When the dehydrated parameters were applied to the air environment microstructural models, parameters of HV/VP-SEM were used as the representative values for the dehydrated SEM environment in the XFEM study since they were identical for both models.

2.6. Sensitivity analysis of the critical damage strains

To understand the sensitivity of the model results to each critical damage strain, a parametric study was conducted. For each model 1–12 in Table 3, each critical damage strain parameter was varied, one-by-one, ±10% from the corresponding baseline value, resulting in 10 new cases, as shown in Table 4. The parametric study thus consisted of 132 simulations performed on 12 microstructural models with 11 cases of different parameter combinations, i.e., one baseline model plus ten models with one critical damage strain modified as shown in Table 4.

3. Results

3.1. Critical damage strains determination

The determined local critical damage initiation strains, ε^0, of cortical bone tested in air, HV-SEM, VP-ESEM, and WV-ESEM environments, using three micro-CT representative slices for the air environment and one slice for the other environments, are listed in Table 5. These values were obtained based on the assumption that the cement line interfaces have ~50% of the critical strain energy release rate of the surrounding tissue (Ural and Mischinski, 2013; Yadav et al., 2021). The load-displacement curves in the linear elastic region, shown in Fig. 2, and crack patterns, shown in Figs. 3m-o,v,w, and r, obtained from the models were in good agreement with experimental results. The critical damage strains of the air models in fully hydrated conditions were 0.070 for ε^0_m and ε^0_o, and 0.060–0.061 for ε^0 of the cement lines, whereas those of the dehydrated SEM models were about half the values, namely 0.030–0.040 for ε^0_m and ε^0_o, and 0.010–0.030 for ε^0 of the cement lines. The ε^0 of the cement lines were consistently lower than ε^0_m and ε^0_o by 0.010–0.020 for all environments. When the initial notch tip was at the cement line, as shown in Fig. 3g, the air 1 model required $\varepsilon^0_{cq\text{-}n}$ and $\varepsilon^0_{cq\text{-}s}$

Table 4
Cases representing parameter changes from the baseline values listed in Table 6 to investigate the impact of ε^0 on both the initiation and propagation of a crack in various test environments.

Case number	ε^0_m	ε^0_o	ε^0_{cm}	$\varepsilon^0_{cq\text{-}n}$	$\varepsilon^0_{cq\text{-}s}$
1	10 % ↓	–	–	–	–
2	10 % ↑	–	–	–	–
3	–	10 % ↓	–	–	–
4	–	10 % ↑	–	–	–
5	–	–	10 % ↓	–	–
6	–	–	10 % ↑	–	–
7	–	–	–	10 % ↓	–
8	–	–	–	10 % ↑	–
9	–	–	–	–	10 % ↓
10	–	–	–	–	10 % ↑

Table 5
Evaluated ε^0 values for the matrix, osteons, and cement lines in various test environments.

Model number	Environment	ε^0_m	ε^0_o	ε^0_{cm}	$\varepsilon^0_{cq\text{-}n}$	$\varepsilon^0_{cq\text{-}s}$
1	Air 1	0.070	0.070	0.060	0.061	0.061
2	Air 2	0.070	0.070	0.060	0.060	0.060
3	Air 3	0.070	0.070	0.060	0.060	0.060
7	HV-SEM	0.040	0.040	0.030	0.030	0.030
8	VP-ESEM	0.040	0.040	0.030	0.030	0.030
9	WV-ESEM	0.030	0.030	0.010	0.010	0.010

Critical damage initiation strains: ε^0_m – interstitial matrix for the MAXPE criterion, ε^0_o – osteons for the MAXPE criterion, ε^0_{cm} – cement lines for the MAXPE criterion, $\varepsilon^0_{cq\text{-}n}$ – cement lines for the QUADE criterion in normal direction, $\varepsilon^0_{cq\text{-}s}$ – cement lines for the QUADE criterion in shear direction.

to be slightly higher than ε^0_{cm} by 0.001 so that the crack deviated away from the cement line due to the MAXPE criterion after some growth along the cement line, as observed during testing and shown in Fig. 3a. Compared to that, when the tips of the notches of the HV-SEM and the VP-ESEM models were at the interface, as shown in Figs. 3j and k, there was no modification of ε^0_{cm}, $\varepsilon^0_{cq\text{-}n}$, and $\varepsilon^0_{cq\text{-}s}$ required because the cracks did not deviate from the original path and they grew along the cement lines, as shown in Figs. 3d and e.

3.2. Critical damage strains in different environments

Based on the evaluated ε^0 values in Table 5, the crack profile results for models 10–12 in which dehydration was simulated by using the ε^0 values for the SEM environments are shown in Figs. 3s-u. Similarly, crack profile results of models 4–6 in which hydration was simulated by using the ε^0 values for the air environments are shown in Figs. 3p–r. The applied critical damage strain values for each model are listed in Table 6.

As observed in the experiments, cracks in the simulated hydrated state were much shorter than in the dehydrated state due to the significantly higher fracture resistance. When the initial notch was near, or at, a cement line, cracks in hydrated samples followed or penetrated the cement lines while cracks in the dehydrated state always grew along the cement lines. Crack paths for the WV-ESEM microstructure model did not change with the different analysis conditions as the initial notch shown in Fig. 3l was relatively far away from the cement lines so that the paths were not affected at crack initiation, as shown in Figs. 3r–1,2.

The fracture resistance in terms of K_J at crack initiation was calculated in the same way as for the experiments by using the measured crack extensions in mode I and the values for all models were compared with the previously reported experimental group trends (Shin et al., 2022) – drawn as dashed lines – in Fig. 4, where triangles represent the experimentally determined K_J values, and circles the numerically calculated K_J values using the various models 1–12. In Fig. 4a, the experimental sample (triangle) fell below the average trend line and within the scatter band. Models 1–3 were constructed based on micro-CT scans of that sample and the model results are all close to the experimental result. The results for models 4–6 represent simulated hydration of samples that were originally tested in a dehydrated state in an SEM. Fig. 4a shows that by changing the critical damage strains to represent typical values of the hydrated condition, those model results fall on each side of the average experimental trendline. In Fig. 4b, models 10–12 represent the inverse case where simulated dehydration was applied to samples that were originally tested in a hydrated state and the model results all fall near the average trendlines observed for dehydrated experimental samples. In all cases, the predicted results match the group trends within ±20 % of the average trendlines for their corresponding critical damage strains. This indicates the applicability of the critical damage strains deduced in Table 5 for simulating hydrated versus dehydrated test conditions.

3.3. Influence of the critical damage strains

The calculated stress intensity factors, K_J, as a function of crack extension are compared with experimental group trends in Fig. 5. To account for variability in the fracture resistance of human cortical bone, bands are plotted for all hydrated air and dehydrated SEM environment experimental data including all data from the ESEM tests. For most cases, the effect of a ±10% change in a critical strain value results in a negligible effect on K_J. Table 7 and Table 8 summarize the 22 cases where the change in K_J was greater than ±10% compared to the corresponding baseline results indicating an effect proportionally larger than the imposed change in the critical strain value. Of these 22 cases, the 10 cases that resulted in crack path changes are listed in Table 7, and the 12 cases that did not result in crack path changes are listed in

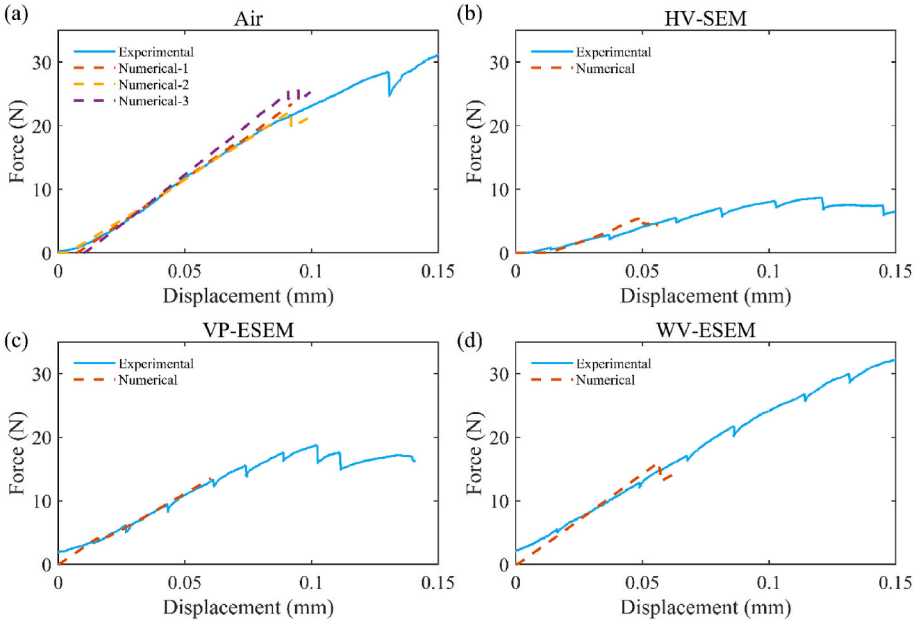

Fig. 2. Load-displacement curve comparisons of experimental and numerical study results for models tested in (a) Air, (b) HV-SEM, (c) VP-ESEM, and (d) WV-ESEM. Solid lines represent experiments and dashed lines numerical data.

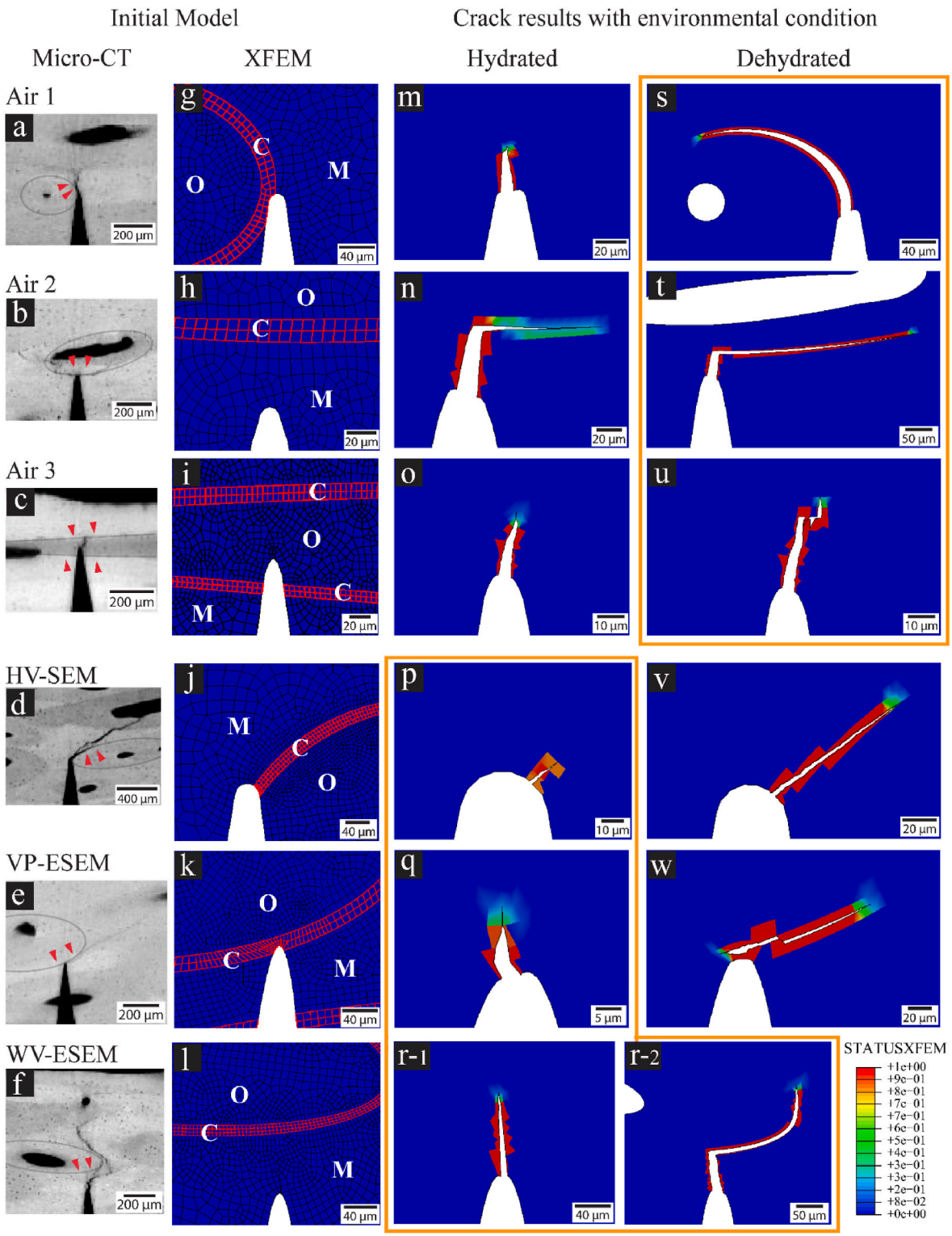

Fig. 3. (a–f) Crack path images obtained from micro-CT scans after crack resistance curve testing in various environments with the estimated cement lines near the initial notches indicated by the grey circle and red arrows. (g–l) Meshes of the corresponding numerical models. The different phases are indicated as: O – osteons, M – interstitial matrix, and C – cement lines that are highlighted in red. (m–r) Crack propagation prediction results for the hydrated air models 1–6 (Table 3) and (s-w,r) for the dehydrated SEM models 7–12 (Table 3) shown as STATUSXFEM maps. (r-1,2) The WV-ESEM model prediction results were the same for the hydrated air and the dehydrated SEM environments; (r-1) shows the initial crack and (r-2) shows an extended crack of (r-1) beyond the elastic region to confirm crack path predictability. The results from the predictions in the different environments are encircled with orange boxes. The STATUSXFEM maps indicate the extent of damage to an element with 0 and 1 representing no damage and complete failure of an element, respectively.

Table 6
Sets of baseline models with ε^0 values for each phase and environment. The ε^0 values that were iteratively determined for the hydrated case are shown for models 1–3. The ε^0 values that were iteratively determined for the dehydrated case are shown for models 7–9. Models 4–6 have been artificially hydrated by raising the ε^0 values of models 7–9, respectively. Models 10–12 have been artificially dehydrated by lowering the ε^0 values of models 1–3, respectively.

XFEM study environment	Model number	Experiment environment	Matrix	Osteons	Cement lines		
			ε^0_m	ε^0_o	ε^0_{cm}	$\varepsilon^0_{cq\text{-}n}$	$\varepsilon^0_{cq\text{-}s}$
Hydrated Air	1	Air 1	0.070	0.070	0.060	0.061	0.061
	2	Air 2	0.070	0.070	0.060	0.060	0.060
	3	Air 3	0.070	0.070	0.060	0.060	0.060
	4	HV-SEM	0.070	0.070	0.060	0.061	0.061
	5	VP-ESEM	0.070	0.070	0.060	0.061	0.061
	6	WV-ESEM	0.070	0.070	0.060	0.061	0.061
Dehydrated SEM	7	HV-SEM	0.040	0.040	0.030	0.030	0.030
	8	VP-ESEM	0.040	0.040	0.030	0.030	0.030
	9	WV-ESEM	0.030	0.030	0.010	0.010	0.010
	10	Air 1	0.040	0.040	0.030	0.030	0.030
	11	Air 2	0.040	0.040	0.030	0.030	0.030
	12	Air 3	0.040	0.040	0.030	0.030	0.030

Critical damage initiation strains: ε^0_m – interstitial matrix for the MAXPE criterion, ε^0_o – osteons for the MAXPE criterion, ε^0_{cm} – cement lines for the MAXPE criterion, $\varepsilon^0_{cq\text{-}n}$ – cement lines for the QUADE criterion in normal direction, $\varepsilon^0_{cq\text{-}s}$ – cement lines for the QUADE criterion in shear direction.

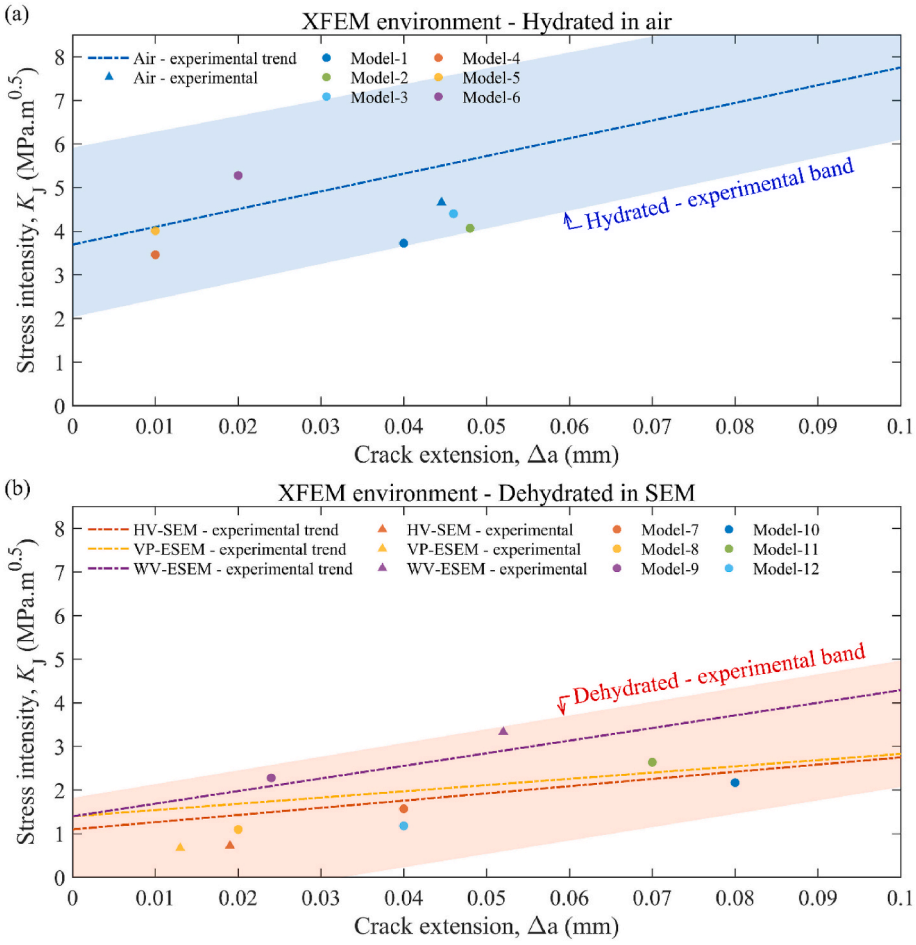

Fig. 4. Fracture resistance predictions for the numerical models listed in Table 3 are plotted as circles. Experimental results used to generate the models for each condition are additionally plotted as triangles and the average trendlines for each test environment are represented as dashed lines; blue for hydrated in air, purple for WV-ESEM, yellow for VP-ESEM, orange for the HV-SEM groups. The trendlines all represent linear fits from experimentally determined data. Additionally, group bands containing all K_J values obtained from experiments in air and the SEM test environments are shown in blue and red, respectively.

Table 8. When the crack path didn't change, K_J typically increased with an increase of ε^0 and decreased with a decreasing ε^0, and this was independent of the phase (osteon, matrix, cement line) that triggered the change. In contrast, crack path changes were only triggered by changes in the ε^0 values for the cement lines. Additionally, because crack path changes involved a competition between two critical strains, the direction of the K_J change did not always match the direction of the ε^0 change. Overall, K_J changes were generally larger when the crack path changed compared to an unchanged crack path, which highlights the larger impact of the cement line critical strains on the crack path.

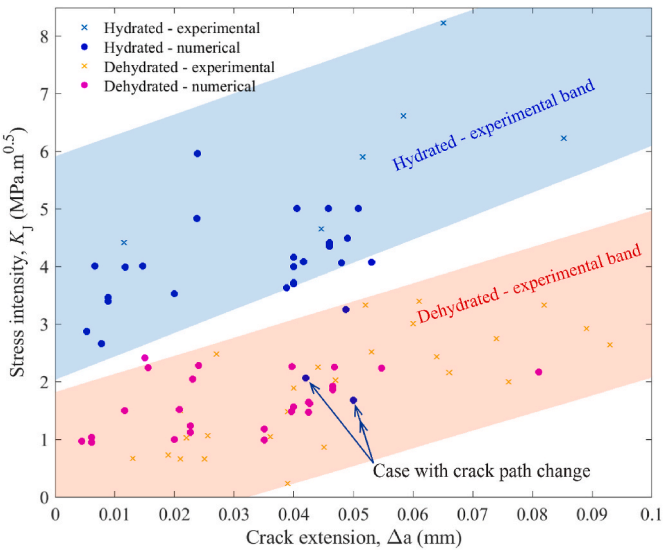

Fig. 5. Predicted stress intensity, K_J, values from computational models with sets of $\mathcal{E}^0$ varied by ±10% (circles) and experiments (x) tested hydrated in air and dehydrated in the various SEM environments (HV-SEM, VP-ESEM, and WV-ESEM). Group bands containing all K_J values obtained from hydrated experiments in air and the dehydrated SEM test environments are shown in blue and red, respectively. Three cases with crack path changes are indicated with blue arrows. The K_J value of two of three cases was the same.

Indeed, among all phase parameters, $\mathcal{E}^0_{cm}$ showed the biggest impact on stress intensity when considering the number of cases impacted by more than ±10% by each parameter change.

Only five cases for the hydrated air environment and one case for the dehydrated SEM environment moved outside of the corresponding scatter band in Fig. 5 and those cases are denoted as "out of band" in Tables 7 and 8. Among those six "out of band" cases, three cases showed the same crack paths as their baseline models and a moderate change in K_J of around 20–27%. Two of these cases barely moved outside the scatter band in Fig. 5. In contrast, for the case of baseline model 3 (see Table 6), increasing $\mathcal{E}^0_o$ by 10% resulted in a K_J decrease of 22% and that drop was sufficient to fall into the dehydrated SEM experimental scatter band (near the upper boundary, as shown in Fig. 5). For this model, the initial notch tip lied entirely within an osteon, as shown in Fig. 3i, and thus $\mathcal{E}^0_o$ seemed to have a significant impact on the stress intensity at crack initiation within that osteon.

The remaining three "out of band" cases corresponded to baseline models 1 and 2 and the crack paths changed significantly as shown in Fig. 6 with the K_J values decreasing by ~50–70% which brought them well into the dehydrated SEM environment experimental scatter band. The initial notch tip of the baseline model 1 sample was located between the cement line and interstitial matrix, as shown in Fig. 6b. For the baseline model matching the experimental crack path, the crack grew along the cement line until it deviated into the matrix, as shown in Fig. 6e. This indicates the active cement line damage criteria has changed from the QUADE to the MAXPE so that the crack grew in the normal direction to the cement line. However, when the $\mathcal{E}^0_{cm}$ and $\mathcal{E}^0_{cq\text{-}n}$ were varied by +10% and −10%, respectively, the MAXPE criterion was not satisfied so that the crack path remained along the cement line similar to experiments and models in the dehydrated SEM condition, as shown in Fig. 6f. This resulted in a ~70% K_J drop. Compared to that, the notch tip of baseline model 2 was in the matrix with the cement line located ahead of the notch root perpendicular to the plane of the notch, as shown in Fig. 6d. In the baseline model matching the experimental crack path, the crack grew straight in the mode I direction and deflected when it encountered the cement line as shown in Fig. 6g. This deflection is caused by the QUADE criterion for the cement line and decreasing $\mathcal{E}^0_{cm}$ by 10% activated the MAXPE criteria for the cement line, so the crack penetrated the cement line as shown in Fig. 6h. This resulted in a K_J drop by 46%. For all three of these cases where a crack path change was observed by changing $\mathcal{E}^0_{cm}$ or $\mathcal{E}^0_{cq\text{-}n}$ by only 10%, the change in fracture resistance was nominally similar to switching from a hydrated to a dehydrated test environment (Fig. 5), showing the relative sensitivity of the model to the cement line critical strains.

The impact of $\mathcal{E}^0$ in the shear direction of cement lines was relatively less significant since varying $\mathcal{E}^0_{cq\text{-}s}$ resulted in no noticeable crack path changes (Fig. 7). For baseline model 4 (see Table 6), the case 9 crack extension increased relative to the baseline when decreasing $\mathcal{E}^0_{cq\text{-}s}$ by 10% (compare Figs. 7c and d), but this resulted in a reduced K_J that remained in the experimental scatter band for the hydrated environment shown in Fig. 5. The inverse case can be seen for baseline model 7 where decreasing $\mathcal{E}^0_{cm}$ by 10% resulted in a slight path change and less crack extension due to a change in the active criteria from QUADE to MAXPE, as shown in Figs. 7e and f. However, once again the K_J increase was well within the dehydrated experimental scatter band shown in Fig. 5.

4. Discussion

4.1. Critical strain values

The results in Table 5 provide quantitative estimates the local damage parameters that control the initiation and propagation of cracks in both hydrated and dehydrated environments that are challenging to measure directly. Giner et al. evaluated $\mathcal{E}^0$ values for sheep tibia that were hydrated and tested in air for cracking in the C–R orientation, i.e., using a crack plane rotated 90° relative to our experiments and models (Giner et al., 2017). Giner et al. determined $\mathcal{E}^0$ values of 0.06–0.08 for the matrix and cement lines. These values are similar to our results for

Table 7
Sets of critical damage strains when the contribution of the parameter variance on the fracture toughness, K_J was greater than ±10% with a crack path change compared to the corresponding baseline results.

Cases with crack path change								
Environment	Model	$\mathcal{E}^0_m$	$\mathcal{E}^0_o$	$\mathcal{E}^0_{cm}$	$\mathcal{E}^0_{cq\text{-}n}$	$\mathcal{E}^0_{cq\text{-}s}$	K_J variance (%)	Out of band[a]
Hydrated Air	1	0.070	0.070	0.060	0.055 (↓10%)	0.061	−69%	Yes
	1	0.070	0.070	0.066 (↑10%)	0.061	0.061	−68%	Yes
	2	0.070	0.070	0.054 (↓10%)	0.060	0.060	−46%	Yes
	5	0.070	0.070	0.066 (↑10%)	0.061	0.061	−21%	
	5	0.070	0.070	0.054 (↓10%)	0.061	0.061	−20%	
	5	0.070	0.070	0.060	0.055 (↓10%)	0.061	−27%	
Dehydrated SEM	7	0.040	0.040	0.027 (↓10%)	0.030	0.030	+43%	
	8	0.040	0.040	0.027 (↓10%)	0.030	0.030	+82%	
	8	0.040	0.040	0.030	0.033 (↑10%)	0.030	+82%	
	10	0.040	0.040	0.027 (↓10%)	0.030	0.030	+35%	

↑↓±10% in the parenthesis indicates parameter variance from the baseline values listed in Table 6.
[a] indicates predicting condition bands shown in Fig. 5.

hydrated samples in air; however, they found a value of 0.12 for the osteon which is approximately twice the values found in the present study. The reason for the difference in the determined osteon critical damage strain can be attributed to the lack of a QUADE criterion using normal and shear principal strains for cement line debonding as they only used the MAXPE criterion for their continuum damage approach. As such, higher values are required for the osteon so that a crack grows along the cement line and does not penetrate the osteon.

To test this hypothesis, model 2 was additionally analyzed without applying the QUADE criterion, and the results are compared in Fig. 8. In the baseline model in the hydrated condition, initially the crack grew along the maximum crack driving force (mode I) direction, as shown in Fig. 8c, and eventually deflected along a cement line, as shown in Fig. 8d. Simply removing the QUADE criterion from the damage criteria for cement lines, while keeping ε^0 values of the baseline model in the hydrated condition, allowed the crack to cross the cement line and propagate into the osteon, as shown in Fig. 8e. This resulted in a significant decrease in K_J compared to the the case where the crack deflected at the cement line, as shown in Fig. 8d. Subsequently, determining the ε^0 values to the measured load displacement curve and K_J

Table 8
Sets of critical damage strains when the contribution of the parameter variance on the fracture toughness, K_J was greater than ±10% without a crack path change compared to the corresponding baseline results.

Cases without crack path change								
Environment	Model	ε^0_m	ε^0_o	ε^0_{cm}	$\varepsilon^0_{cq\text{-}n}$	$\varepsilon^0_{cq\text{-}s}$	K_J variance (%)	Out of band[a]
Hydrated Air	2	0.070	0.070	0.060	0.066 (↑10%)	0.060	+19%	
	3	0.070	0.063 (↓10%)	0.060	0.060	0.060	−22%	Yes
	4	0.070	0.070	0.060	0.061	0.055 (↓10%)	−21%	
	5	0.070	0.063 (↓10%)	0.060	0.061	0.061	−27%	Yes
	6	0.063 (↓10%)	0.070	0.060	0.061	0.061	−15%	
Dehydrated SEM	8	0.040	0.040	0.030	0.030	0.027 (↓10%)	−12%	
	8	0.040	0.040	0.030	0.030	0.033 (↑10%)	+50%	
	8	0.040	0.040	0.030	0.027 (↓10%)	0.030	−18%	
	9	0.033 (↑10%)	0.030	0.010	0.010	0.010	+20%	Yes
	11	0.036 (↓10%)	0.040	0.030	0.030	0.030	−16%	
	11	0.044 (↑10%)	0.040	0.030	0.030	0.030	+15%	
	12	0.040	0.036 (↓10%)	0.030	0.030	0.030	−12%	

↑↓±10% in the parenthesis indicates parameter variance from the baseline values listed in Table 6.
[a] indicates predicting condition bands shown in Fig. 5.

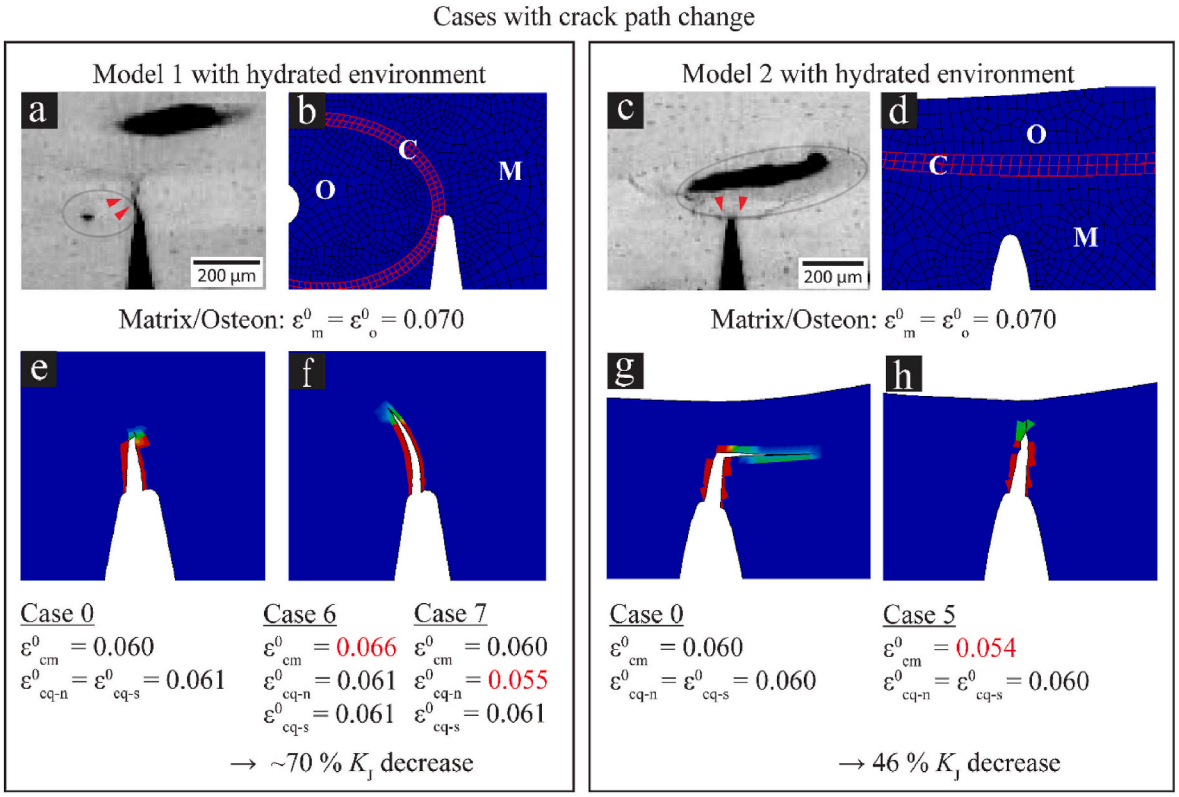

Fig. 6. Crack propagation patterns and K_J results for models that were significantly impacted by ±10% ε^0 variations. (a, c) Micro-CT image with the estimated cement lines near the initial notch indicated by the grey circle and red arrows. (b, d) Baseline models 1 and 2 models in the hydrated condition. The different phases are indicated as: O – osteons, M – interstitial matrix, and C – cement lines that are highlighted in red. (e, g) STATUSXFEM damage indicating maps show the crack path predictions of baseline models and (f, h) for the ±10% ε^0 variation case models showing the crack path changes. The STATUSXFEM maps indicate the extent of damage to an element with 0 and 1 representing no damage and complete failure of an element, respectively. Sets of ε^0 values used for the analyses are listed below the corresponding crack images. Varied parameter values from the baselines are indicated in red.

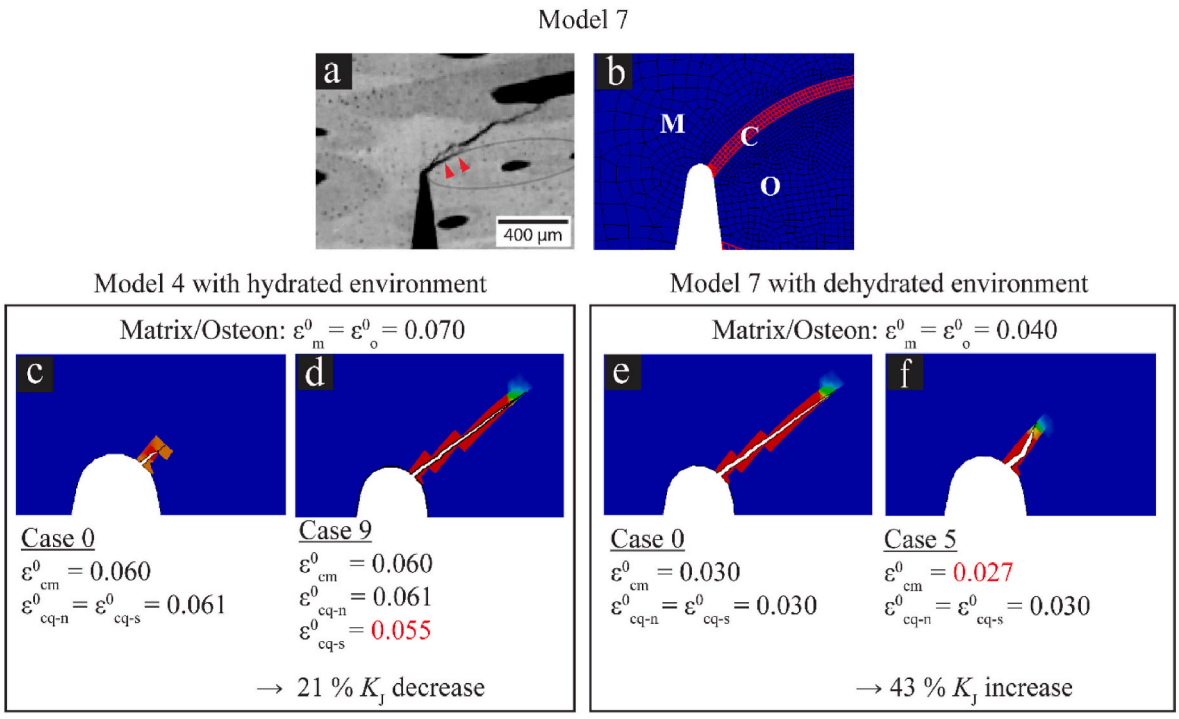

Fig. 7. Crack propagation patterns and K_J changes resulting from ±10% ε^0 variations from corresponding baseline models. (a) Micro-CT image with the estimated cement lines near the initial notch indicated by the grey circle and red arrows. (b) The model microstructure created from the image in (a). The different phases are indicated as: O – osteons, M – interstitial matrix, and C – cement lines that are highlighted in red. (c, e) STATUSXFEM damage indicating maps show the crack path predictions of baseline models and (d, f) for the ±10% ε^0 variation case models. The STATUSXFEM maps indicate the extent of damage to an element with 0 and 1 representing no damage and complete failure of an element, respectively. The sets of ε^0 values used for the analyses are listed below the corresponding crack images. Varied parameter values from the baselines are indicated in red.

value without the QUADE criterion yielded a value of 0.11 for the osteons, i.e., similar to (Giner et al., 2017), while the other values were unchanged. However, the determined model was limited to the point where the crack remains in the maximum crack driving force (mode I) direction, as shown in Fig. 8c. Without the QUADE criterion, the crack deflection observed in experiments could not be reproduced. Instead, the crack was arrested by the osteon, preventing further propagation under the same applied displacement, as shown in Fig. 8f. This indicates the critical role of the QUADE criterion in governing crack propagation along the cement lines.

In the XFEM damage model study by Gustafsson et al. which included the QUADE criterion, a theoretical single osteon model was analyzed under tension and QUADE criterion-based ε^0 values of 0.0015–0.00008 were reported for the cement lines (Gustafsson et al., 2019a). Compared to the present study, those values are a relatively smaller fraction of the ε^0 values for the osteons and matrix which were fixed to be 0.004 in (Gustafsson et al., 2019a). The relatively lower QUADE criterion-based ε^0 values in their work are attributed to their assumption of a relatively higher elastic modulus for cement lines compared to matrix and osteon, which is based on the study of Skedros et al. (Milovanovic et al., 2018; Skedros et al., 2005) that argued that cement lines are hyper-mineralized compared to the surrounding bone tissue.

To test this hypothesis, the assumption of relatively higher elastic modulus of cement lines was investigated with model 2. From the original baseline conditions of model 2, the elastic modulus combinations were replaced with similar values to the study of Gustafsson et al. (Gustafsson et al., 2019a), as indicated below the image in Fig. 9d, and the model was determined for ε^0 values to predict the experimental result. This reduced the ε^0 value for the QUADE criterion of cement lines from 0.060 to 0.020, which was necessary to prevent the crack from crossing the cement line, as shown in Fig. 9d. This makes the MAXPE criterion-based ε^0 values three times higher than those for the QUADE criterion when the elastic modulus of cement lines exceeded that of the surrounding materials. This is consistent with Gustafsson et al.'s study results, where MAXPE criterion-based ε^0 values of 0.004 were roughly three times higher than the QUADE criterion-based ε^0 value of 0.0015. Furthermore, the overall lower magnitudes of the values can be attributed to them fixing the MAXPE criterion-based ε^0 values to be 0.004.

Recent reported nanoindentation results have consistently found a relatively lower elastic modulus of ~10 GPa for cement lines compared to ~20 GPa for the osteon and matrix of bovine, ovine, and human cortical bone (Montalbano and Feng, 2011; Yadav et al., 2021; Zhou et al., 2020). We therefore suggest that a small difference in ε^0 between phases is likely to be the realistic scenario when the elastic moduli of each phase from previously reported nanoindentation studies are used. Nonetheless, even if one assumes that the cement lines are hyper-mineralized and have a higher modulus, the mineral content will still be bound together by organic components that will be affected by dehydration.

4.2. *Hydrated vs. dehydrated conditions*

The results in Table 5 indicate that the SEM-induced dehydration lowered the overall critical damage initiation strain by about half. For the hydrated samples tested in air, it is estimated that they would have lost ~3% water by mass, including pore and bound water, based on work by Nyman et al. (2013). The loss of loosely collagen-bound water is associated with embrittlement under dehydration conditions (Broz et al., 1993; Nyman et al., 2006, 2013, 2013; Yan et al., 2008; Melvin and Evans, 1973; Kahler et al., 2003; Shin et al., 2022; Li et al., 2013; Abdel-Wahab et al., 2012; Vergani et al., 2014; Burr, 2019; Samuel et al., 2014, 2016; Utku et al., 2008). While the exact water content could not be measured during the SEM experiments, most of the water was removed from the tissue to achieve the vacuum pressure levels in Table 1 since the SEM will not permit operation if the sample is still heavily outgassing. The significant reduction in fracture toughness observed in

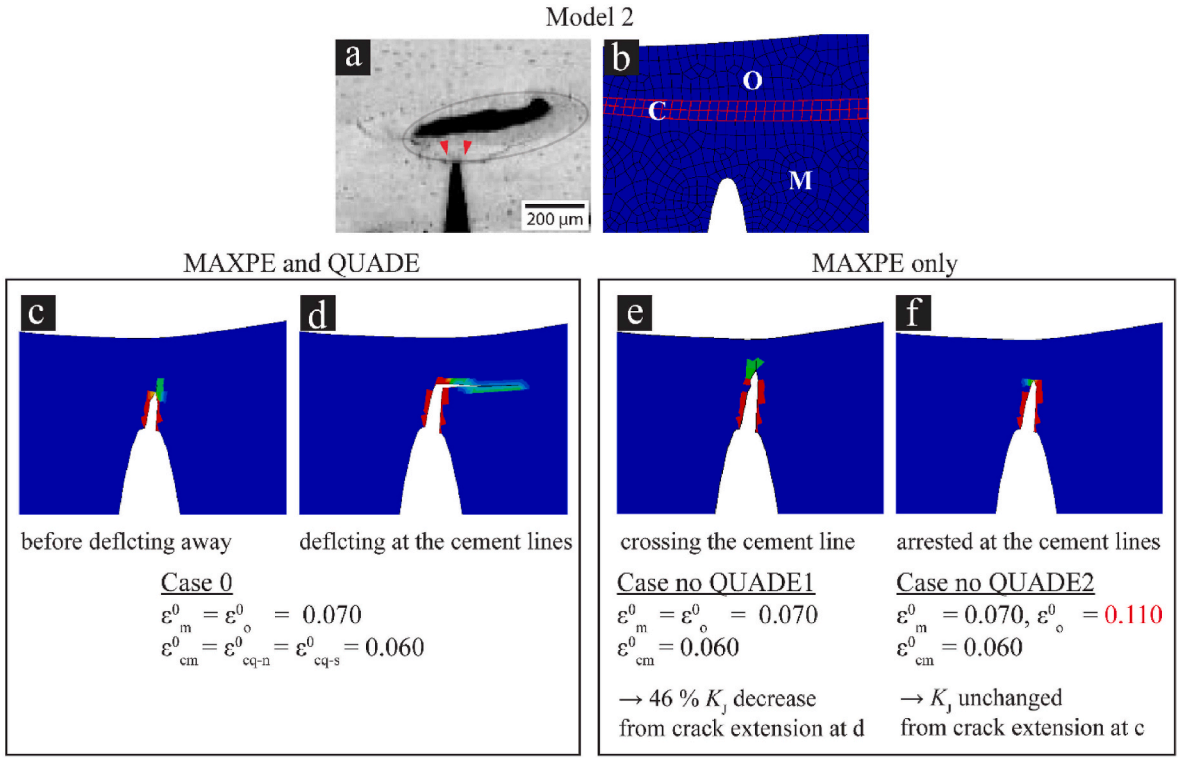

Fig. 8. Crack propagation patterns and K_J changes resulting from eliminating the QUADE criterion from the corresponding baseline model 2. (a) Micro-CT image with the estimated cement lines near the initial notch indicated by the grey circle and red arrows. (b) The model microstructure created from the image in (a). The different phases are indicated as: O – osteons, M – interstitial matrix, and C – cement lines that are highlighted in red. STATUSXFEM damage indicating maps show progressive crack path predictions of (c, d) the baseline model and (e, f) for the cases without the QUADE criterion. The STATUSXFEM maps indicate the extent of damage to an element with 0 and 1 representing no damage and complete failure of an element, respectively. The sets of ε^0 values used for the analyses are listed below the corresponding crack images. Varied parameter values from the baselines are indicated in red.

the SEM condition indicates a loss of collagen-bound and pore water compared to the samples tested in air due to SEM-induced embrittlement. This embrittlement corresponds to a reduction in the critical damage strains deduced for our XFEM models and less frequent phase changes of the crack paths observed in our experiments. When a crack was deflected by changing its path from one phase to another, crack growth was more difficult due to the higher energy requirement to redirect the crack, which is a main toughening mechanism for our cracking orientation that requires transversely cutting through the osteons (Zimmermann et al., 2009). Similar to Gustafsson et al. (2019b), crack path changes from one phase to another were accommodated in our models by a competition of two criteria: the MAXPE criterion to resist the maximum crack driving force and the QUADE criterion to resist the interface force in the cement lines. The QUADE criterion, which allows crack growth along the cement lines, was dominantly active in the dehydrated condition due to the relatively low values of ε^0 compared to those in the hydrated condition. Whenever a crack encountered the cement lines, it tended to grow along them in the dehydrated condition, which resulted in longer cracks. Compared to that, in the hydrated air condition, ε^0 of the interface was often sufficiently large to resist debonding resulting in crack path changes towards the maximum crack driving force direction. For the VP-ESEM model shown in Fig. 3k, for example, the initial notch tip was at the cement line, which was aligned nearly perpendicular to the direction of the highest crack driving force. Switching this model to use the hydrated critical damage strains causes the crack to initiate at and cross the cement line due to the highest crack driving force being in that direction, as shown in Fig. 3q. The same model in dehydrated conditions exhibited crack initiation and propagation along the cement line (Fig. 3w), similar to what was observed in the experiment (Fig. 3e). In the dehydrated condition, debonding and crack propagation along the cement line seems to be a dominant mechanism rather than penetrating and crossing cement lines which occurs more frequently in the hydrated condition.

The experimentally observed crack paths in the hydrated condition were replicated through simulations using the determined sets of critical strain values in models 1, 2, and 3, while those in the dehydrated conditions were replicated in models 7, 8, and 9. Initially, an equal value for the QUADE and MAXPE criteria of the cement lines was assumed. However, in model 1 with the hydrated environment, a slightly higher value of ε^0 was required for the QUADE criterion compared to the MAXPE criterion of cement lines. This adjustment was necessary to accurately predict the experimentally observed crack paths. However, overall, a relatively minor ~15% reduction of the cement line QUADE and MAXPE ε^0 values compared to the osteons and matrix ε^0 values appears sufficient for predicting the experimentally observed crack paths in the hydrated condition. In contrast, it was observed that a slightly larger mismatch of 25–33% between the ε^0 values for the cement lines and the surrounding materials improved the prediction of experimentally observed crack paths in the dehydrated environments. This illustrates how relatively subtle changes in the ratios between the critical damage strains from the hydrated condition can give rise to significantly different crack propagation behavior, an observation that was further supported by the parametric study results.

Of the six models showing significant K_J changes in the parametric study, five models corresponded to ε^0 values in hydrated conditions, as listed in Tables 7 and 8. Even with small changes in ε^0 of cement lines in the hydrated condition, crack paths were changed and resulted in a significant decrease in K_J. In contrast, when the resistance to the cement line crack path was changed by variation in ε^0 of the cement lines in the dehydrated condition, the K_J value only slightly increased. This suggests that hydrated bone is more sensitive to the competition between the various ε^0 parameters than dehydrated bone where the competition is

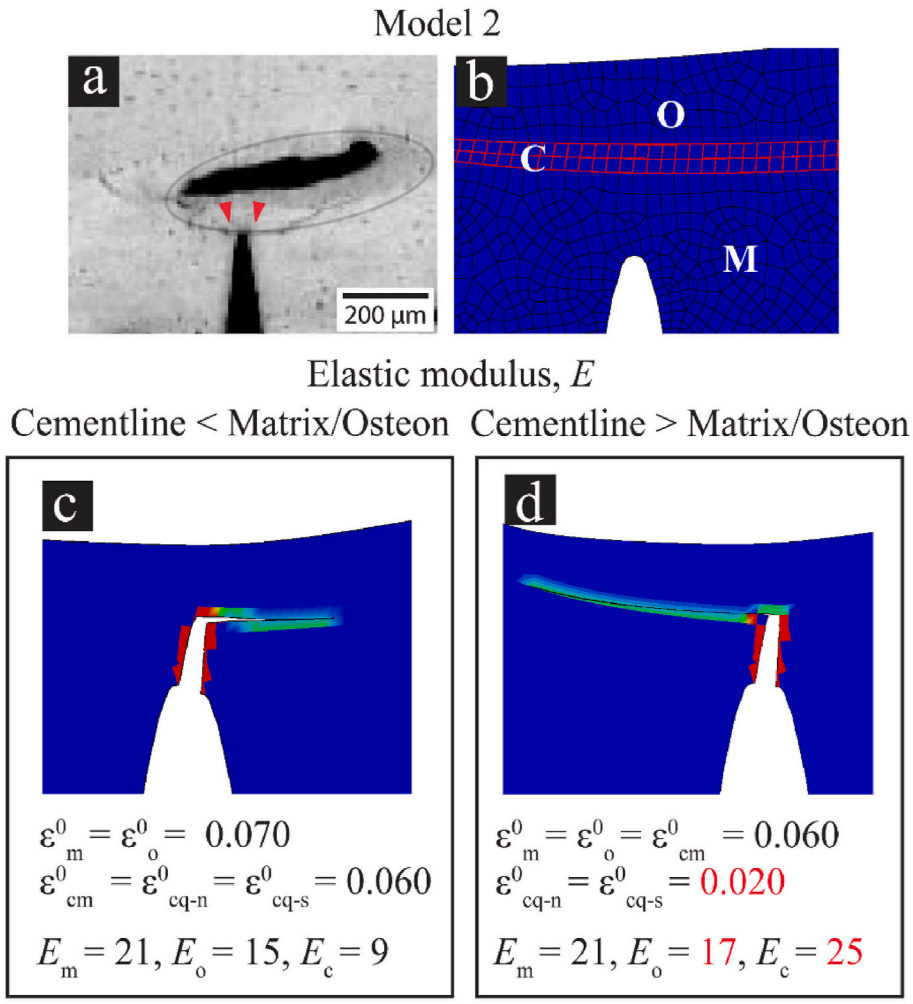

Fig. 9. Crack propagation patterns of model 2 resulting from *E* variations from the corresponding baseline model. (a) Micro-CT image with the estimated cement lines near the initial notch indicated by the grey circle and red arrows. (b) The model microstructure created from the image in (a). The different phases are indicated as: O – osteons, M – interstitial matrix, and C – cement lines that are highlighted in red. STATUSXFEM damage indicating maps show the crack path predictions of (c) the baseline model and (d) for the *E* variation case model. The STATUSXFEM maps indicate the extent of damage to an element with 0 and 1 representing no damage and complete failure of an element, respectively. The sets of ε^0 and *E* values used for the analyses are listed below the corresponding crack images. Varied parameter values from the baselines are indicated in red.

heavily skewed towards cement line propagation.

Even when a crack path change was induced by a slight change in ε^0, the fracture toughness values generally stayed within the scatter band seen in Fig. 5. An example of this can be seen in Fig. 10 where selected parametric study results are compared for models 1 and 10, both of which used the same microstructural model. In the hydrated condition, the experimental and simulated cracks both started to grow along the cement line according to the QUADE criterion, and after some growth, the path deviated as the strain fields near the crack tip changed to satisfy the MAXPE criterion, as shown in Fig. 10c. After ±10% changes in the ε^0 of the cement lines (cases 6 and 7), the influence of the QUADE criterion became larger than the MAXPE criterion, which resulted in no phase change of the crack path, as shown in Fig. 10d. This deviation in crack path to the cement line led to a reduction in the K_J value from the hydrated experimental band to the dehydrated band in Fig. 5. A similar crack pattern was observed, but more pronounced, when the same microstructure was analyzed with the dehydrated condition ε^0 values, as shown in Fig. 10e. Furthermore, when the ε^0_{cm} value was changed −10% (case 5) to induce a crack path change, the K_J value increased, as shown in Fig. 10f, but not enough to exhibit hydrated levels of fracture toughness in Fig. 5. This example shows that the critical damage strains for the hydrated condition are just on the edge of maintaining a crack path that gives high fracture toughness, while the critical damage strains for the dehydrated condition generally give low fracture resistance for all phases (Fig. 10f), and they especially promote cement line fracture for most cases as illustrated in Figs. 3s–w and Fig. 3r-2.

4.3. Importance of the cement line critical damage strains

The parametric study revealed that the microstructural condition near the notch root influences the relative impact of each parameter on the crack initiation path and, consequently, the resistance to crack growth and the fracture toughness of the bone. When the notch root was located entirely in either the matrix or the osteon phase and far from a cement line, as shown in Figs. 3i and l, ±10% ε^0 variation of matrix or osteon resulted in ~10–30% changes in K_J; however, K_J remained unchanged even if ε^0 of the cement lines was modified. Compared to that, when the notch tip was located either close to or directly at a cement line, crack initiation was more sensitive to variations of ε^0 of the cement lines with ~20–80% changes in K_J.

The orientation of cement lines with respect to the root of the notch additionally played an important role in the initiation and propagation of cracks. As crack growth in our study was in the L-R testing orientation where cracks primarily grew perpendicular to the longitudinally aligned

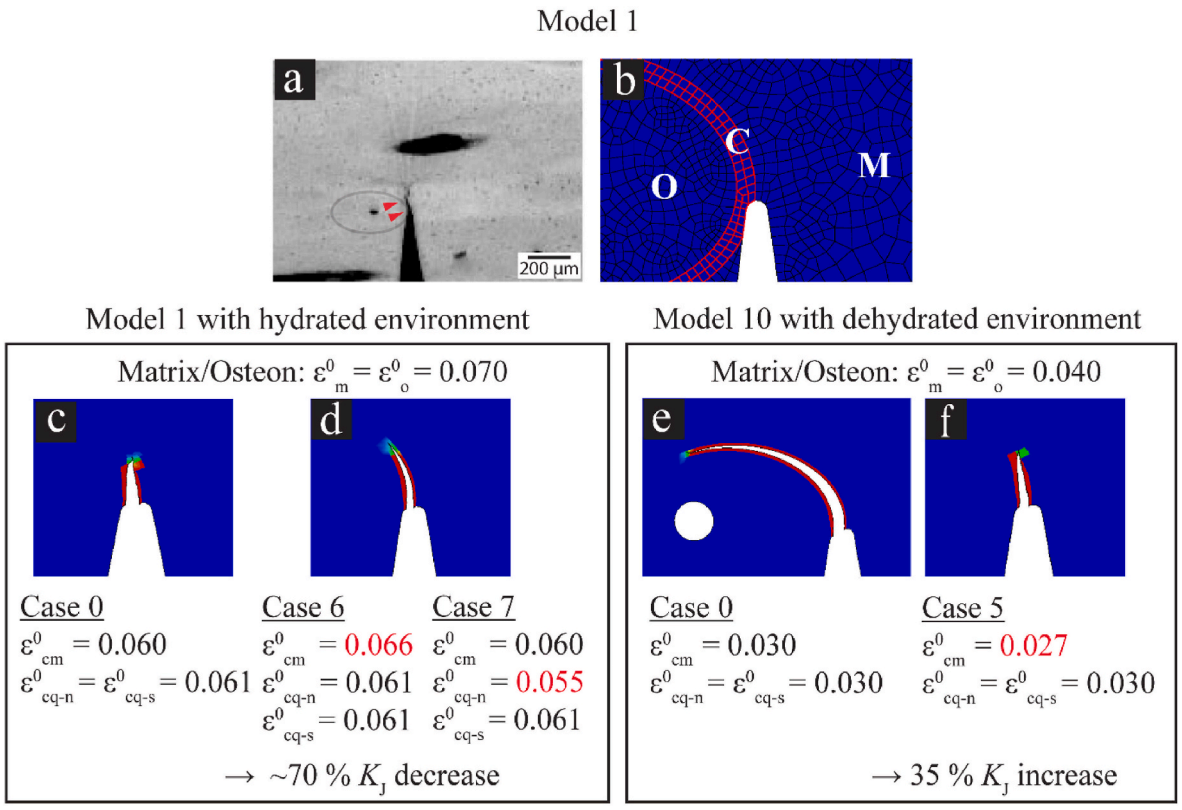

Fig. 10. Crack propagation patterns and K_J changes resulting from ±10% ε^0 variations from the corresponding baseline models. (a) Micro-CT image with the estimated cement lines near the initial notch indicated by the grey circle and red arrows. (b) The model microstructure created from the image in (a). The different phases are indicated as: O – osteons, M – interstitial matrix, and C – cement lines that are highlighted in red. (c, e) STATUSXFEM damage indicating maps show the crack path predictions of baseline models and (d, f) for the ±10% ε^0 variation case models. The STATUSXFEM maps indicate the extent of damage to an element with 0 and 1 representing no damage and complete failure of an element, respectively. The sets of ε^0 values used for the analyses are listed below the corresponding crack images. Varied parameter values from the baselines are indicated in red.

osteons and cement lines, the change in critical damage normal strain mainly influenced the crack path change. Compared to that, the critical damage shear strain change had minimal impact on crack path change (Fig. 7). Similarly, Gustafsson et al. have shown that the impact of critical normal and critical shear strains depends on the applied loading direction with respect to the cement lines (Gustafsson et al., 2019c). Moreover, the most significant changes in crack initiation toughness were caused by changes in the difference between the ε^0_{cm} and $\varepsilon^0_{cq\text{-}n}$ rather than by changes in the individual absolute values. Whenever the active criterion changed from MAXPE to QUADE or from QUADE to MAXPE in the cement lines, the crack path deflected and changed phases, requiring more energy to open the crack and thereby increasing the fracture toughness. This shows the importance of the mismatch between the ε^0 values for the two criteria that control the individual mechanisms of cracking at the cement lines.

While the mismatch between ε^0_{cm} and $\varepsilon^0_{cq\text{-}n}$ significantly impacted the crack path, changes were more often influenced by variations in ε^0_{cm}, as listed in Table 7, where 7 out of 10 crack path changes were caused by variations in ε^0_{cm}. Similar observations were made in the parametric study on numerical crack propagation in the work of Gustafsson et al. (2019c). In their parametric study using the XFEM damage model, they investigated the importance of material properties, including Young's modulus, fracture energy, critical damage strain, and Poisson's ratio of the three phases on four criteria of maximum force, fracture energy, crack length, and crack trajectory using 2D single osteon models in three different orientations under tensile loading. Their findings also showed the largest impact on fracture energy, crack length, and crack path, resulted from changes in ε^0_{cm} as observed in the present study for the hydrated condition. Thus, the ability for the crack to move off the cement line and into another phase is inherently difficult in the hydrated case, and thus the models are most sensitive to the critical strain that controls that cracking mechanism.

Experimental studies of fracture in bone (e.g., Nalla et al., 2006b; Nalla et al., 2004) and recent 3D numerical work using human femur micro-CT images (Demirtas et al., 2023) have repeatedly highlighted the importance of cement lines in the bone fracture process. Furthermore, it has been frequently observed that changes in the crack deflection mechanisms in irradiated, diseased, or aged bone lead to lower fracture resistance compared to healthy bone (Barth et al., 2011; Carlton et al., 2010; Koester et al., 2011; Carriero et al., 2014; Nalla et al., 2006b). Thus, while the present study focused on the effect of dehydration, it is likely that the effects of irradiation, disease, or age on the fracture process of bone might be controlled similarly by the critical damage strains of the cement lines.

4.4. Limitations of this study

A limitation that must be considered in the XFEM formulation of our framework within Abaqus is that it does not allow cracks to nucleate inside a region that already contains a crack. I.e., an enriched element can only be intersected by one crack, and cracks cannot coalesce. This allows only one crack to propagate, making it hard to simulate phenomena such as crack bifurcation or the coalescence of microcracks in bone. For example, the initial crack bifurcated in the experiments corresponding to Fig. 3a and f, while our current study models could only simulate the dominant crack. Additionally, the three material phases were simplified with representative material properties of each phase instead of modeling the sub-structure, such as layers of the lamella,

microcracks, lacunae, and canaliculi. The 2D microstructure geometry for simulations, particularly that of the cement lines, could not be captured precisely due to the limited micro-CT resolution, and as no histology data was used. While using only a small number of six representative micro-CT slices for this study, the consistency of the study results across different slices taken from a similar test environment suggests the reliability of the data obtained. A larger sample size, i.e., a higher number of slices, should enhance the accuracy of the methodology. Furthermore, we have only scanned data after testing, but not before due to the known impact of irradiation on bone's resistance to the initiation and growth of cracks. As a result, the constructed models for the simulations represent the estimated initial conditions of the samples. Finally, due to the constraints of a 2D model, a crack cannot grow throughout the thickness. Consequently, this study does not account for the 3D effects that may impact crack paths.

5. Conclusion

An XFEM damage model analysis using six representative micro-CT slices in hydrated and dehydrated environments was performed based on the assumption that the cement line interfaces have ~50% of the critical strain energy release rate of the surrounding tissue (Ural and Mischinski, 2013; Yadav et al., 2021) to determine and understand the influence of the local critical damage strains, $\mathcal{E}^0$, on the fracture behavior of human bone samples obtained from a 46-year-old, healthy male during the initiation and early growth of the crack. Based on these computational fracture analysis results, the following conclusions can be made.

- After calibrating the $\mathcal{E}^0$ values, the models were able to accurately predict the fracture toughness at the initial stages of the crack growth resistance curves and the crack paths observed in experiments for both the hydrated and dehydrated environments. Values of $\mathcal{E}^0$ in the hydrated environment were nearly double that of the dehydrated environments.
- Switching the $\mathcal{E}^0$ values in the XFEM model from hydrated to dehydrated values, or vice versa, produced fracture toughness results that corresponded to the environment associated with the new $\mathcal{E}^0$ values rather than the original model. Thus, changes in the critical damage strains appears to be a viable way to use XFEM to interpret the effect of dehydration on the fracture process in bone, and there is scope to apply this approach to study the effects of aging, disease, and medical therapies on bone fracture.
- Experimentally observed crack deflection at the cement lines is driven in the XFEM model by a competition between the MAXPE and QUADE damage criteria, which represent the damage arising from the maximum crack driving force and from the relatively lower toughness of cement line interfaces, respectively.
- Analyses with varied values of $\mathcal{E}^0$ revealed that cracks in hydrated bone mostly try to follow the maximum crack driving force direction with deflections away from the cement lines, which increases the initiation fracture toughness, while cracks in dehydrated bone have the tendency to follow the cement line interfaces due to their lower toughness.
- The $\mathcal{E}^0$ values of the cement lines appear to impact the crack growth resistance and crack paths more significantly in the hydrated environments since a small change in $\mathcal{E}^0$ can influence the crack path to give a significant reduction in crack growth resistance. In contrast, the critical damage strains for the dehydrated condition are far from what is required to give high toughness and small deviations from the dehydrated $\mathcal{E}^0$ values do not have a large impact on the dehydrated model results.

Overall, the XFEM damage model and the local critical damage initiation strains were found to provide valuable insight into understanding crack initiation and propagation mechanisms in different hydration states at the microstructural level.

Funding

This research did not receive any specific grant from funding agencies in the public, commercial, or not-for-profit sectors. TS acknowledges funding from NSF Award 1952993.

CRediT authorship contribution statement

Mihee Shin: Writing – review & editing, Writing – original draft, Visualization, Methodology, Investigation, Data curation. **Penny J. Martens:** Writing – review & editing, Supervision. **Thomas Siegmund:** Writing – review & editing, Methodology. **Jamie J. Kruzic:** Writing – review & editing, Supervision, Methodology, Conceptualization. **Bernd Gludovatz:** Writing – review & editing, Validation, Supervision, Project administration, Methodology, Conceptualization.

Declaration of competing interest

The authors declare that they have no known competing financial interests or personal relationships that could have appeared to influence the work reported in this paper.

Data availability

Data will be made available on request.

Acknowledgements

BG acknowledges support of the UNSW Scientia Fellowship scheme, and TS acknowledges funding from NSF Award 1952993.

Appendix A. Supplementary data

Supplementary data to this article can be found online at https://doi.org/10.1016/j.jmbbm.2024.106468.

References

Abdel-Wahab, A.A., Maligno, A.R., Silberschmidt, V.V., 2012. Micro-scale modelling of bovine cortical bone fracture: analysis of crack propagation and microstructure using X-FEM. Comput. Mater. Sci. 52, 128–135. https://doi.org/10.1016/j.commatsci.2011.01.021.

ASTM E1823-20a, 2020. Standard Terminology Relating to Fatigue and Fracture Testing. ASTM International.

ASTM Standard E1820, 2020. Standard Test Method for Measurement of Fracture Toughness. ASTM International.

Barth, H.D., Zimmermann, E.A., Schaible, E., Tang, S.Y., Alliston, T., Ritchie, R.O., 2011. Characterization of the effects of x-ray irradiation on the hierarchical structure and mechanical properties of human cortical bone. Biomaterials 32, 8892–8904. https://doi.org/10.1016/j.biomaterials.2011.08.013.

Belytschko, T., Black, T., 1999. Elastic crack growth in finite elements with minimal remeshing. Int. J. Numer. Methods Eng. 45 (5), 601–620. https://doi.org/10.1002/(SICI)1097-0207(19990620)45:5<601::AID-NME598>3.0.CO;2-S.

Belytschko, T., Moës, N., Usui, S., Parimi, C., 2001. Arbitrary discontinuities in finite elements. Int. J. Numer. Methods Eng. 50 (4), 993–1013. https://doi.org/10.1002/1097-0207(20010210)50:4<993::AID-NME164>3.0.CO;2-M.

Broz, J.J., Simske, S.J., Greenberg, A.R., Luttges, M.W., 1993. Effects of rehydration state on the flexural properties of whole mouse long bones. J. Biomech. Eng. 115, 447–449. https://doi.org/10.1115/1.2895510.

Burr, D.B., 2019. Changes in bone matrix properties with aging, 120. Elsevier, pp. 85–93. https://doi.org/10.1016/j.bone.2018.10.010. Bone.

Carlton, H., Launey, M., Macdowell, A., Ager, J., Ritchie, R., 2010. On the effect of X-ray irradiation on the deformation and fracture behavior of human cortical bone. Bone 46 (6), 1475–1485. https://doi.org/10.1016/j.bone.2010.02.025.

Carriero, A., Zimmermann, E.A., Paluszny, A., Tang, S.Y., Bale, H., Busse, B., Alliston, T., Kazakia, G., Ritchie, R.O., Shefelbine, S.J., 2014. How tough is brittle bone? Investigating osteogenesis imperfecta in mouse bone. J. Bone Miner. Res. 29, 1392–1401. https://doi.org/10.1002/jbmr.2172.

Demirtas, A., Taylor, E.A., Gludovatz, B., Ritchie, R.O., Donnelly, E., Ural, A., 2023. An integrated experimental-computational framework to assess the influence of microstructure and material properties on fracture toughness in clinical specimens of

human femoral cortical bone. J. Mech. Behav. Biomed. Mater. 145, 145. https://doi.org/10.1016/j.jmbbm.2023.106034, 106034.
Giner, E., Belda, R., Arango, C., Vercher-Martínez, A., Tarancón, J.E., Fuenmayor, F.J., 2017. Calculation of the critical energy release rate Gc of the cement line in cortical bone combining experimental tests and finite element models. Eng. Fract. Mech. 184, 168–182. https://doi.org/10.1016/j.engfracmech.2017.08.026.
Granke, M., Does, M.D., Nyman, J.S., 2015. The role of water compartments in the material properties of cortical bone. Calcif. Tissue Int. 97, 292–307. https://doi.org/10.1007/s00223-015-9977-5.
Gustafsson, A., Khayyeri, H., Wallin, M., Isaksson, H., 2019a. An interface damage model that captures crack propagation at the microscale in cortical bone using XFEM. J. Mech. Behav. Biomed. Mater. 90, 556–565. https://doi.org/10.1016/j.jmbbm.2018.09.045.
Gustafsson, A., Wallin, M., Isaksson, H., 2019b. Age-related properties at the microscale affect crack propagation in cortical bone. J. Biomech. 95, 109326 https://doi.org/10.1016/j.jbiomech.2019.109326.
Gustafsson, A., Wallin, M., Khayyeri, H., Isaksson, H., 2019c. Crack propagation in cortical bone is affected by the characteristics of the cement line: a parameter study using an XFEM interface damage model. Biomech. Model. Mechanobiol. 18, 1247–1261. https://doi.org/10.1007/s10237-019-01142-4.
Kahler, B., Swain, M.V., Moule, A., 2003. Fracture-toughening mechanisms responsible for differences in work to fracture of hydrated and dehydrated dentine. J. Biomech. 36, 229–237. https://doi.org/10.1016/S0021-9290(02)00327-5.
Koester, K., Carlton, H., Ritchie, R., 2011. Effect of aging on the transverse toughness of human cortical bone: evaluation by R-curves. J. Mech. Behav. Biomed. Mater. 4, 1504–1513. https://doi.org/10.1016/j.jmbbm.2011.05.020.
Li, S., Abdel-Wahab, A., Demirci, E., Silberschmidt, V.V., 2013. Fracture process in cortical bone: X-FEM analysis of microstructured models. Int. J. Fract. 184, 43–55. https://doi.org/10.1007/s10704-013-9814-7.
Lin, Z.X., Xu, Z.H., An, Y.H., Li, X., 2016. In situ observation of fracture behavior of canine cortical bone under bending. Mater. Sci. Eng. C 62, 361–367. https://doi.org/10.1016/j.msec.2016.01.061.
Lucksanasombool, P., Higgs, W.A.J., Higgs, R.J.E.D., Swain, M.V., 2001. Fracture toughness of bovine bone: influence of orientation and storage media. Biomaterials 22, 3127–3132. https://doi.org/10.1016/S0142-9612(01)00062-X.
Maghsoudi-Ganjeh, M., Wang, X., Zeng, X., 2020. Computational investigation of the effect of water on the nanomechanical behavior of bone. J. Mech. Behav. Biomed. Mater. 101, 103454 https://doi.org/10.1016/j.jmbbm.2019.103454.
Marco, M., Belda, R., Miguélez, M.H., Giner, E., 2018. A heterogeneous orientation criterion for crack modelling in cortical bone using a phantom-node approach. Finite Elem. Anal. Des. 146, 107–117. https://doi.org/10.1016/j.finel.2018.04.009.
MATLAB. Version 9.9.0 (R2020b), 2020. The MathWorks Inc., Natick, Massachusetts.
McCalden, R.W., McGlough, J.A., Barker, M.B., Court-Brown, C.M., 1993. Age-related changes in the tensile properties of cortical bone. The relative importance of changes in porosity, mineralization and microstructure. J. Bone Joint Surg. - Series A 75 (8), 1193–1205. https://doi.org/10.2106/00004623-199308000-00009.
Melenk, J.M., Babuška, I., 1996. The partition of unity finite element method: basic theory and applications. Comput. Methods Appl. Mech. Eng. 139 (1–4), 289–314. https://doi.org/10.1016/S0045-7825(96)01087-0.
Melvin, J.W., Evans, F.G., 1973. Crack Propagation in Bone, Biomechanics Symposium ASME, pp. 87–88. New York.
Milovanovic, P., Scheidt, A., Mletzko, K., Sarau, G., Püschel, K., Djuric, M., Amling, M., Christiansen, S., Busse, B., 2018. Bone tissue aging affects mineralization of cement lines. Bone 110, 187–193. https://doi.org/10.1016/j.bone.2018.02.004.
Mischinski, S., Ural, A., 2011. Finite element modeling of microcrack growth in cortical bone. J. Appl. Mech., Trans. ASME 78 (4), 041016. https://doi.org/10.1115/1.4003754.
Montalbano, T., Feng, G., 2011. Nanoindentation characterization of the cement lines in ovine and bovine femurs. J. Mater. Res. 26 (8), 1036–1041. https://doi.org/10.1557/jmr.2011.46.
Nalla, R.K., Kruzic, J.J., Kinney, J.H., Ritchie, R.O., 2004. Effect of aging on the toughness of human cortical bone: evaluation by R-curves. Bone 35 (6), 1240–1246. https://doi.org/10.1016/j.bone.2004.07.016.
Nalla, R.K., Balooch, M., Ager, J.W., Kruzic, J.J., Kinney, J.H., Ritchie, R.O., 2005. Effects of polar solvents on the fracture resistance of dentin: role of water hydration. Acta Biomater. 1 (1), 31–43. https://doi.org/10.1016/j.actbio.2004.08.002.
Nalla, R.K., Kinney, J.H., Tomsia, A.P., Ritchie, R.O., 2006a. Role of alcohol in the fracture resistance of teeth. J. Dent. Res. 85, 1022–1026. https://doi.org/10.1177/154405910608501109.
Nalla, R.K., Kruzic, J.J., Kinney, J.H., Balooch, M., Ager, J.W., Ritchie, R.O., 2006b. Role of microstructure in the aging-related deterioration of the toughness of human cortical bone. Mater. Sci. Eng. 26, 1251–1260. https://doi.org/10.1016/j.msec.2005.08.021.
Nyman, J.S., Roy, A., Shen, X., Acuna, R.L., Tyler, J.H., Wang, X., 2006. The influence of water removal on the strength and toughness of cortical bone,. J. Biomech. 39 (5), 931–938. https://doi.org/10.1016/j.jbiomech2005.01.012.
Nyman, J.S., Gorochow, L.E., Adam Horch, R., Uppuganti, S., Zein-Sabatto, A., Manhard, M.K., Does, M.D., 2013. Partial removal of pore and loosely bound water by low-energy drying decreases cortical bone toughness in young and old donors. J. Mech. Behav. Biomed. Mater. 22, 136–145. https://doi.org/10.1016/j.jmbbm.2012.08.013.
O'Brien, F.J., Taylor, D., Clive Lee, T., 2007. Bone as a composite material: the role of osteons as barriers to crack growth in compact bone. Int. J. Fatig. 29 (6), 1051–1056. https://doi.org/10.1016/j.ijfatigue.2006.09.017.
Pereira, F.A.M., Morais, J.J.L., de Moura, M.F.S.F., Dourado, N., Dias, M.I.R., 2012. Evaluation of bone cohesive laws using an inverse method applied to the DCB test. Eng. Fract. Mech. https://doi.org/10.1016/j.engfracmech.2012.10.002, 96724-736.
Samuel, J., Sinha, D., Zhao, J.C.G., Wang, X., 2014. Water residing in small ultrastructural spaces plays a critical role in the mechanical behavior of bone. Bone 59, 199–206. https://doi.org/10.1016/j.bone.2013.11.018.
Samuel, J., Park, J.S., Almer, J., Wang, X., 2016. Effect of water on nanomechanics of bone is different between tension and compression. J. Mech. Behav. Biomed. Mater. 57, 128–138. https://doi.org/10.1016/j.jmbbm.2015.12.001.
Shin, M., Zhang, M., Scheidt, A., Pelletier, M.H., Walsh, W.R., Martens, P.J., Kruzic, J.J., Busse, B., Gludovatz, B., 2022. Impact of test environment on the fracture resistance of cortical bone. J. Mech. Behav. Biomed. Mater. 129. https://doi.org/10.1016/j.jmbbm.2022.105155, 105155.
Skedros, J.G., Holmes, J.L., Vajda, E.G., Bloebaum, R.D., 2005. Cement lines of secondary osteons in human bone are not mineral-deficient: new data in a historical perspective. Anat. Rec. Part A Discoveries in Molecular, Cellular, and Evolutionary Biology 286, 781–803. https://doi.org/10.1002/ar.a.20214.
Smith, N.W., Ekwaro-Osire, S., Khandaker, M., Hashemi, J., 2011. Influence of storage duration on retention of original fracture toughness. Exp. Mech. 51, 697–705doi. https://doi.org/10.1007/S11340-010-9370-0.
Tamilselvan, A., Zhang, D., 2002. Effect of bone water content on fracture resistance of bone. Proceedings of the IEEE Annual Northeast Bioengineering Conference. NEBEC, pp. 199–200.
Tang, T., Ebacher, V., Cripton, P., Guy, P., McKay, H., Wang, R., 2015. Shear deformation and fracture of human cortical bone. Bone 71, 25–35. https://doi.org/10.1016/j.bone/2014.10.001.
Ural, A., 2020. Advanced modeling methods—applications to bone fracture mechanics. Curr. Osteoporos. Rep. 18, 568–576. https://doi.org/10.1007/S11914-020-00615-1.
Ural, A., Mischinski, S., 2013. Multiscale modeling of bone fracture using cohesive finite elements. Eng. Fract. Mech. 103, 141–152. https://doi.org/10.1016/j.engfracmech.2012.05.008.
Utku, F.S., Klein, E., Saybasili, H., Yucesoy, C.A., Weiner, S., 2008. Probing the role of water in lamellar bone by dehydration in the environmental scanning electron microscope. J. Struct. Biol. 162 (3), 361–367doi. https://doi.org/10.1016/j.jsb.2008.01.004.
Vergani, L., Colombo, C., Libonati, F., 2014. In: Crack propagation in cortical bone: a numerical study. Procedia Mater. Sci. 3, 1524–1529. https://doi.org/10.1016/j.mspro.2014.06.246.
Weiner, S., Wagner, H.D., 1998. The material bone: structure-mechanical function relations. Annu. Rev. Mater. Sci. 28 (1), 271–298. https://doi.org/10.1146/annurev.matsci.28.1.271.
Yadav, R.N., Uniyal, P., Sihota, P., Kumar, S., Dhiman, V., Goni, V.G., Sahni, D., Bhadada, S.K., Kumar, N., 2021. Effect of ageing on microstructure and fracture behavior of cortical bone as determined by experiment and Extended Finite Element Method (XFEM). Med. Eng. Phys. 93, 100–112. https://doi.org/10.1016/j.medengphy.2021.05.021.
Yan, J., Daga, A., Kumar, R., Mecholsky, J.J., 2008. Fracture toughness and work of fracture of hydrated, dehydrated, and ashed bovine bone. J. Biomech. 41 (9), 1929–1936doi. https://doi.org/10.1016/j.jbiomech.2008.03.037.
Zhou, Y., Kastner, M.J., Tighe, T.B., Du, J., 2020. Elastic modulus mapping for bovine cortical bone from submillimeter- to submicron-scales using PeakForce Tapping atomic force microscopy. Extreme Mech Lett 41, 41. https://doi.org/10.1016/j.eml.2020.101031, 101031.
Zimmermann, E.A., Launey, M.E., Barth, H.D., Ritchie, R.O., 2009. Mixed-mode fracture of human cortical bone. Biomaterials 30, 5877–5884. https://doi.org/10.1016/j.biomaterials.2009.06.017.
Zimmermann, E.A., Launey, M.E., Ritchie, R.O., 2010. The significance of crack-resistance curves to the mixed-mode fracture toughness of human cortical bone. Biomaterials 31, 5297–5305. https://doi.org/10.1016/j.biomaterials.2010.03.056.